








RESEARCH ARTICLE | MARCH 08 2024

Driven electron g -factor anisotropy in layered III–V semiconductors: Interfacing, tunnel coupling, and structure inversion asymmetry effects

M. A. Toloza Sandoval   ; J. E. Leon Padilla  ; A. B. Wanderley  ; G. M. Sipahi  ; J. F. Diniz Chubaci  ; A. Ferreira da Silva 

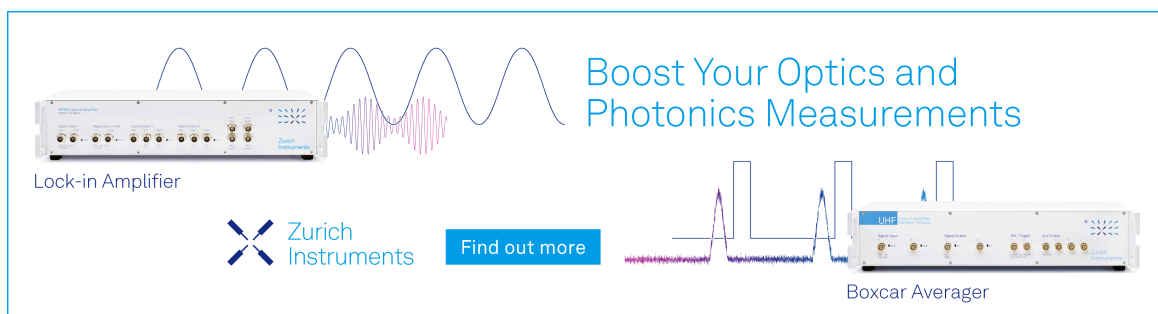
 Check for updates

J. Appl. Phys. 135, 103901 (2024)

<https://doi.org/10.1063/5.0187962>




CrossMark



Boost Your Optics and Photonics Measurements

Lock-in Amplifier

 Zurich Instruments

[Find out more](#)

Boxcar Averager

Driven electron g -factor anisotropy in layered III-V semiconductors: Interfacing, tunnel coupling, and structure inversion asymmetry effects

Cite as: J. Appl. Phys. **135**, 103901 (2024); doi: [10.1063/5.0187962](https://doi.org/10.1063/5.0187962)

Submitted: 17 November 2023 · Accepted: 21 February 2024 ·

Published Online: 8 March 2024



M. A. Toloza Sandoval,^{1,2,3,a)} J. E. Leon Padilla,³ A. B. Wanderley,⁴ G. M. Sipahi,⁴ J. F. Diniz Chubaci,⁵ and A. Ferreira da Silva^{3,5,6}

AFFILIATIONS

¹Illum School of Science, Brazilian Center for Research in Energy and Materials, 13083-970 Campinas, São Paulo, Brazil

²Brazilian Nanotechnology National Laboratory, Brazilian Center for Research in Energy and Materials, 13083-100 Campinas, São Paulo, Brazil

³Institute of Physics, Federal University of Bahia, 40210-340 Salvador, Bahia, Brazil

⁴São Carlos Institute of Physics, University of São Paulo, 13566-590 São Carlos, São Paulo, Brazil

⁵Laboratory of Ionic Crystals, Thin Films and Dating, Institute of Physics, University of São Paulo, 05508-090 Butantã, São Paulo, Brazil

⁶Multuser Nanotechnology Laboratory, Northeast Center for Strategic Technologies, 50740-540 Recife, Brazil

^{a)}Author to whom correspondence should be addressed: marcelo.sandoval@lnnano.cnpem.br

ABSTRACT

A key piece for spintronic applications, the so-called electron g -factor engineering is still predominantly based on the semiconductor bulk g factor and its dependence on the bandgap energy. In nanostructures, however, the mesoscopic confinement introduces exclusive anisotropies, transforming scalar g factors into tensors, enabling different renormalization mechanisms as routes for fine-tuning the electron g factor. These questions we address in this comparative theoretical analysis between the obtained electron g -factor (tensor) anisotropies for realistic InAs|AlSb- and In_{0.53}Ga_{0.47}As|InP-based multilayers. The electron g -factor anisotropy, i.e., the difference between g factors for magnetic fields parallel and perpendicular to the interfaces, is analytically calculated via perturbation theory using the envelope-function approach based on the eight-band Kane model. Effects from bulk, interfacing, tunnel coupling, and structure inversion asymmetry are systematically introduced within a transparent comparative view; differences between obtained anisotropies, such as in the magnitude, sign, and other fine details, are analyzed in terms of the heterostructure parameters, mapped over different confining and tunnel-coupling regimes without requiring elaborated numerical computations.

© 2024 Author(s). All article content, except where otherwise noted, is licensed under a Creative Commons Attribution-NonCommercial 4.0 International (CC BY-NC) license (<http://creativecommons.org/licenses/by-nc/4.0/>). <https://doi.org/10.1063/5.0187962>

I. INTRODUCTION

More than a century ago, the efforts to explain the anomalous Zeeman effect allowed the conception of the electron spin degree of freedom as treated by relativistic quantum mechanics.¹ A triumph of this theory was the prediction of the free electron g factor, $g_0 = 2$, quantifying the anomalous Zeeman effect by using spin-splitting energy on the atomic spectrum in the presence of a static magnetic field. A small contribution to the free electron g factor arises from radiative corrections, described according to

quantum electrodynamics (QED), which predicts a corrected free electron g factor (denoted as g_e to differ from g_0) given in leading order by

$$g_e = 2(1 + \alpha/2\pi) \approx 2.0023, \quad (1)$$

where $\alpha = e^2/\hbar c \approx 1/137$ is the fine-structure constant (e is the electron charge, \hbar is the reduced Planck constant, and c is the speed of light). However, the slight deviation from $g_0 = 2$ is predicted by the QED and measured with extreme accuracy, far

beyond the leading order correction [Eq. (1)], the agreement between theory and experiment stands for a scientific milestone.²

More recently, the continuous improvement in nanomaterial production established a route to manipulate the spin properties in solid-state environments, emerging the spintronics that fastly evolved into a fertile cross-disciplinary field of fundamental and applied research.³ In particular, an intuitive analogy becomes possible in solid-state environments regarding the spin splitting of the electronic energy spectrum in the presence of a static magnetic field—such splitting results from an effective Zeeman interaction by introducing a corresponding effective g factor, according to the effective mass formulation. For example, in III–V semiconductor alloys, the electron g factor is further corrected by bulk band structure effects, varying from ≈ 2.4 , in AlSb, to ≈ -51 in InSb. Such variation can be described, in leading order, by employing the theoretical prescription developed by Roth, Lax, and Zwerdling,⁴

$$g_{bulk}^* = 2 \left(1 - \frac{m_e}{m^*} \frac{\Delta}{3E_g + 2\Delta} \right), \quad (2)$$

where m^* is the electron effective mass in units of the free electron mass m_e , E_g is the fundamental energy bandgap, and Δ is the valence-band spin-orbit (SO) energy splitting. Therefore, in leading order, the electron effective g factor varies in a role inversely proportional to the bulk bandgap energy, such the modulation with the bulk parameters given by Roth's formula provides a cornerstone to engineer the electron g factor by choosing the host material.⁵ For this reason, InAs and other narrow-gap III–V semiconductors present prominent g factors (as well as SO coupling), forming building blocks in platforms of interest for developing spintronic devices,⁶ topological materials,⁷ besides electron g -factor engineering.⁸ In Table I, we show experimental data for different III–V semiconductor alloys and emphasize the deviation of the effective g factor (g^*) from the bare value (g_e), depending on the fundamental bandgap and other bulk parameters. In general, the accuracy of Eq. (2) increases when the bandgap decreases, in excellent agreement for InAs alloys, for example. On the other hand, significant corrections from remote bands are evident for alloys with wider gaps.

Moreover, in nanomaterial and device architectures, the structural details can turn relevant or even operational. Due to abrupt interfaces, scalar g factors can be converted into tensors, with a corresponding anisotropy much investigated in different materials and confining geometries.^{12–29} Despite the progress toward incorporating structural design into g -factor engineering, it still lacks a detailed and transparent understanding of the distinct g -factor

renormalization mechanisms connected with structural details, complementing the Roth formulation for the bulk g factor. Such demand and related questions are addressed in this paper, in which we discuss an analytical extension of the Roth prescription based on the envelope-function approach and use it to calculate the electron g -factor anisotropy (via perturbation theory) in realistic III–V heterostructures. Results for InGaAs/InP- and InAs/AlSb-based multilayers are analyzed within a transparent comparative view, with fine-tuning mechanisms systematically introduced and critical differences explained in terms of the bulk and structural parameters. Next, the theoretical framework will be introduced from a single symmetric active layer, reproducing Roth's formula as bulk limits.

II. LAYERED III-V SEMICONDUCTORS AND THE ELECTRON g -FACTOR TENSOR

Simplest layered III–V semiconductors are formed by a single active layer, with thickness L_w , sandwiched by semiconductors with wider bandgaps that act as confining barriers, described according to the conduction and valence band-edge profiles shown in Fig. 1(a), for the structures labeled. For these symmetric structures, the ground state electron g factor interpolates bulk g factors obeying the well-defined limits shown in Fig. 1(b); this interpolation starts from the bulk g factor of the barrier material (g_{InP}^* or g_{AlSb}^*) when the active layer is sufficiently thin, i.e., for $L_w \rightarrow 0$ and converges to the bulk g factor of the active layer (g_{InGaAs}^* or g_{InAs}^*) when L_w is large enough. Between these bulk limits, the electronic g factor depends on the thickness L_w and the magnetic-field orientation, which is particularly well-defined for the configurations parallel (\mathbf{B}_{\parallel}) and perpendicular (\mathbf{B}_{\perp}) to the interfaces. The corresponding g factors, namely, g_{\parallel}^* and g_{\perp}^* , are components of a g tensor, and the difference $\Delta g^* = g_{\parallel}^* - g_{\perp}^*$ defines a g -factor anisotropy.

To introduce an electron effective g -tensor formulation from a natural extension of the Roth equation to III–V heterostructures within the eight-band $\mathbf{k} \cdot \mathbf{p}$ envelope-function model, we first consider the in-plane magnetic-field configuration (parallel to the interfaces) and the growth direction along the z axis to obtain the g -tensor component by employing first-order perturbation theory in the weak magnetic-field limit,^{26,30,31}

$$g_{\parallel}^* = 2 \left\langle 1 - \frac{m_e}{m(z, \varepsilon_0)} \frac{\Delta(z)}{3\varepsilon_g(z, \varepsilon_0) + 2\Delta(z)} + \frac{2m_e}{\hbar^2} \alpha_R(z, \varepsilon_0) [z - z_0] + \delta_{rem}(z) \right\rangle_{\psi_0}, \quad (3)$$

where

$$m(z, \varepsilon) = \frac{\hbar^2 \varepsilon_g(z, \varepsilon) [\varepsilon_g(z, \varepsilon) + \Delta]}{P^2 3\varepsilon_g(z, \varepsilon) + 2\Delta} \quad (4)$$

is the standard position- and energy-dependent electron effective mass,^{18,32–35} $\varepsilon_g(z, \varepsilon) = \varepsilon - E_c(z) + E_g(z)$ is the effective energy bandgap [noting that $m(z, \varepsilon)$ reduces to $m^* = \frac{\hbar^2 E_g(E_g + \Delta)}{P^2 3E_g + 2\Delta}$ in the bulk limits, setting the Kane matrix element P as usually^{34,36,37}], ε_0 and ψ_0 are the unperturbed solutions, i.e., the electronic ground state

TABLE I. Experimental data for III–V semiconductor bulk-band parameters available in Refs. 5 and 9–11.

	InAs	In _{0.53} Ga _{0.47} As	InP	AlSb
E_g (eV)	0.42	0.81	1.42	2.38
Δ (eV)	0.38	0.33	0.11	0.67
m^* (m_e)	0.023	0.041	0.079	0.13
g^*	-14.9	-4.5	+1.26	+0.84

18 March 2024 14:57:17

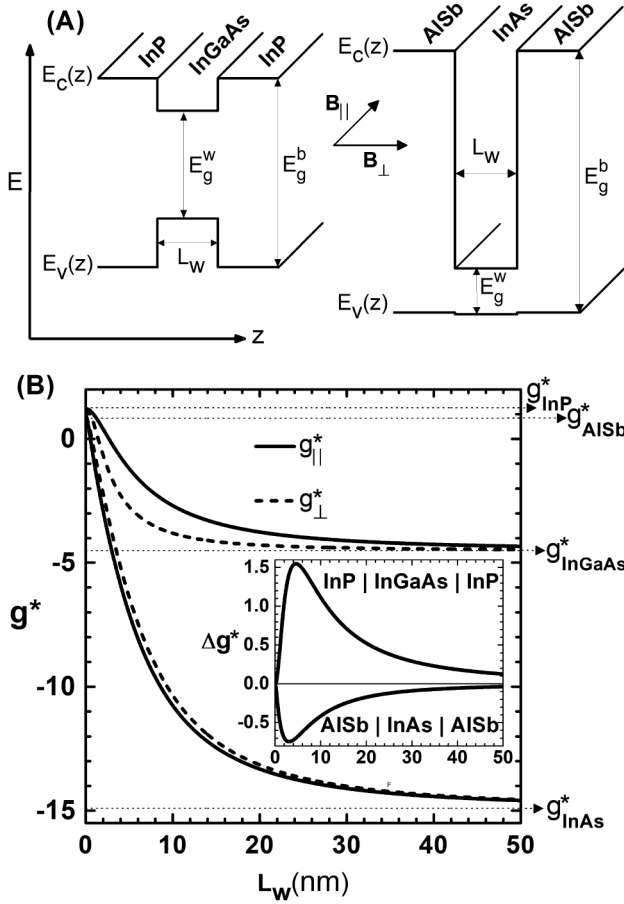


FIG. 1. (a) Bandgap alignments for the heterostructures $\text{InP}|\text{In}_{0.53}\text{Ga}_{0.47}\text{As}|\text{InP}$ and $\text{AlSb}|\text{InAs}|\text{AlSb}$ grown along the z axis: L_w is the thickness of the active layer, $E_c(z)$ is the conduction band-edge profile [$\Delta E_c(\text{InP}|\text{InGaAs}) = 0.26$ eV and $\Delta E_c(\text{AlSb}|\text{InAs}) = 1.98$ eV are the bandoffsets] and $E_v(z)$ is the valence band-edge profile. \mathbf{B}_{\parallel} and \mathbf{B}_{\perp} describe magnetic-field configurations parallel and perpendicular to the interfaces, respectively. (b) Calculated parallel and perpendicular g factors varying with L_w ; horizontal (dotted) lines set the bulk g -factors, and the inset shows the electron g -factor anisotropy. The parameters were used according to Table I.

energy and the corresponding wavefunction for $B = 0$, $z_0 = \langle z \rangle_{\psi_0}$ is the expectation value of the electron's position, $\delta_{rem}(z)$ is the contribution of the remote bands,³⁸ and $\alpha_R(z, \varepsilon) = \frac{d}{dz}\beta(z, \varepsilon)$ is the Rashba SO coupling parameter such that

$$\beta(z, \varepsilon) = \frac{P^2}{2} \left[\frac{1}{\varepsilon_g(z, \varepsilon)} - \frac{1}{\varepsilon_g(z, \varepsilon) + \Delta(z)} \right] \quad (5)$$

is the (standard) position- and energy-dependent SO coefficient,^{32–34,39} for flatband structures as shown in Fig. 1(a), the dependence on z is due to the variation of the band parameters, which change abruptly from one bulk value to another across the interfaces. Therefore, for the magnetic-field configuration above

described, different contributions for the g -tensor component are identified in Eq. (3), allowing a transparent physical interpretation for each term (and the role of the interplay between them); in particular, it is explicit how this g -tensor component comprises the Rashba coupling to describe an effective Zeeman interaction.

On the other hand, the magnetic-field configuration perpendicular to the interfaces preserves the axial symmetry of the heterostructure (note that \mathbf{B}_{\perp} is aligned with the growth direction), and retaining the leading order correction,²⁶ the electron effective g factor can be written as

$$g_{\perp}^* = 2 \left\langle 1 - \frac{m_e}{m(z, \varepsilon_0)} \frac{\Delta(z)}{3\varepsilon_g(z, \varepsilon_0) + 2\Delta(z)} + \delta_{rem}(z) \right\rangle_{\psi_0}; \quad (6)$$

it is the averaged bulk g factor calculated using the zero-order solutions ε_0 and ψ_0 , i.e., $g_{\perp}^* = \langle g_{bulk}^*(z, \varepsilon_0) \rangle_{\psi_0}$, a direct and well-known extension of Roth's formula to includes quantum size effects and corrections from remote bands.⁴⁰ Since this average is spatially isotropic and $g_{\parallel}^* = \langle g_{bulk}^* \rangle_{\psi_0} + \Delta g^*$, it is straightforwardly recognized that

$$\Delta g^* = (4m_e/\hbar^2) \langle \alpha_R(z, \varepsilon_0) [z_0 - z] \rangle_{\psi_0}; \quad (7)$$

i.e., it is the principal electron g -factor anisotropy in heterostructures with strong SO coupling. It is easy to check that Eq. (7) leads to the usual Rashba SO interaction in the zero magnetic-field limit;⁴¹ however, under the presence of an in-plane magnetic field, $\langle \alpha_R(z, \varepsilon_0) z \rangle_{\psi_0}$ assumes finite values even for symmetric heterostructures (contrastingly with the usual Rashba effect). Considering the structures shown in Fig. 1(a), for example, the interfaces give reminiscent contributions to solve Eq. (7), $\beta(z, \varepsilon_0)$ can be written in terms of step functions, and the electron g -factor anisotropy depends crucially on the difference $\delta\beta(\varepsilon_0) = \beta_w(\varepsilon_0) - \beta_b(\varepsilon_0)$. It is then easy to solve Eq. (7) to find

$$\Delta g^* = (4m_e/\hbar^2) L_w |\psi_0(z_i)|^2 \delta\beta(\varepsilon_0), \quad (8)$$

which is positive or negative, depending on $\delta\beta(\varepsilon_0)$. Such dependence is observed in Fig. 1(b), in which we consider the structures labeled in Fig. 1(a) with the parameters shown in Table I. For these heterostructures, the anisotropy vanishes in the bulk limits, $L_w = 0$ and L_w large enough, since Δg^* depends on the probability density at interfaces ($|\psi_0(z_i)|^2$), according to Eq. (7).

Such a simple and transparent formulation for the g -factor anisotropy was successfully employed for different III–V single active-layer structures¹⁸—in remarkable agreement with independent experimental works. This study was then extended to multilayers based on (lattice-matched) $\text{InP}|\text{In}_{0.47}\text{Ga}_{0.53}\text{As}$, including tunnel coupling between active layers and structure inversion asymmetry (SIA) effects.²⁶ Such acquired knowledge suits here as a benchmark in a comparative analysis with another typical heterostructure: $\text{AlSb}|\text{InAs}$ multilayers belong to the family 6.1 Å and, due to the narrow-gap InAs active layer, allow a pronounced g -factor modulation (from $g_{\text{AlSb}}^* = 0.84$ to $g_{\text{InAs}}^* = -14.9$), as shown in Fig. 1, where other peculiar features are already understood, as $\Delta g \leq 0$ (i.e., $g_{\parallel} \leq g_{\perp}$) and its reduced magnitude due to the large band offset, which suppresses the probability density at the interfaces. In Secs. III–VI, we will introduce and discuss tunnel

coupling and structure inversion asymmetry within a systematic procedure, comparing the obtained results for the abovementioned structures, showing how the theoretical framework can comprise different renormalization mechanisms that affect the g -factor anisotropy and how it depends on specific details for each heterostructure.

III. TUNNEL-COUPLED ACTIVE LAYERS

We extend our study to structures with tunnel-coupled active layers, introducing a central barrier formed by the same material as the lateral barriers. Figure 2(a) provides a schematic view, where L_w is the thickness of the active layers, and L_b is the width of the tunnel barrier. Setting the growth direction along the z -axis, we chose the origin of the coordinate system at the inversion symmetry center such that $\psi_0(z) = \psi_0(-z)$. It reduces our analysis to two nonequivalent interfaces, z_{i_l} locates the interface between the active layer and the lateral barrier, and z_{i_c} is between the active layer and the central barrier. Such (unperturbed) solutions, discussed in detail in Ref. 36, are shown for specific multilayers in Fig. 2(b). In a similar procedure to that introduced in Sec. II, it is easy to solve Eq. (6) considering such a multilayer parameterization using the space spanned by confining and tunnel-coupling parameters, L_w and L_b , as follows:

$$\Delta g^* = (4m_e/\hbar^2) \{ 2L_w |\psi_0(z_{i_l})|^2 + L_b [|\psi_0(z_{i_l})|^2 - |\psi_0(z_{i_c})|^2] \} \delta\beta(\epsilon_0). \quad (9)$$

Thereby, specifying the heterostructure, we compute Δg^* for each point of the space spanned to construct a contour-plot map.

In Fig. 3, we present the contour-plot maps within a high-contrast comparative view, according to the color legend shown on the right. With $\Delta g^* \geq 0$, the upper surface and its projection (on the top panel) map the anisotropy over the whole parameter space for InP|In_{0.53}Ga_{0.47}As|InP|In_{0.53}Ga_{0.47}As|InP. To contrast, in the lower landscape (with surface and projection), we present the corresponding results for AlSb|InAs|AlSb|InAs|AlSb multilayer structures, for which $\Delta g^* \leq 0$. As in Sec. II, the sign of the g -factor anisotropy is determined by $\delta\beta(\epsilon_0)$.

Other significant features of the obtained anisotropy maps arise when introducing a tunnel-coupling layer between active layers, explained according to Eq. (9). Starting from the single active-layer limit $L_b = 0$, within the strongly interacting regime for L_b thin, the anisotropy is reduced due to the difference between probability densities at nonequivalent interfaces, i.e., $|\psi_0(z_{i_l})|^2 - |\psi_0(z_{i_c})|^2 \leq 0$. This difference vanishes for L_b large enough, such that the system reproduces two non-interacting active layers, with a total anisotropy $\Delta g^* = 2(4m_e/\hbar^2)L_w|\psi_0(z_{i_l})|^2\delta\beta$. The features exposed by the landscapes show how structural parameterization affects the system when it passes through different confining and coupling domains. Analyzing Δg^* when L_b increases, InAs|AlSb-based structures quickly achieve the non-interacting regime (with stable value for Δg^*), given the tunnel coupling is drastically reduced due to the large conduction-band offset, as shown in Fig. 2(b); in contrast, because of the smaller band offset, InGaAs|InP-based structures comport a larger interacting domain when compared with those based on InAs|AlSb. It explains the dependence of Δg^* on L_b evidenced in upper and lower landscapes shown in Fig. 3.

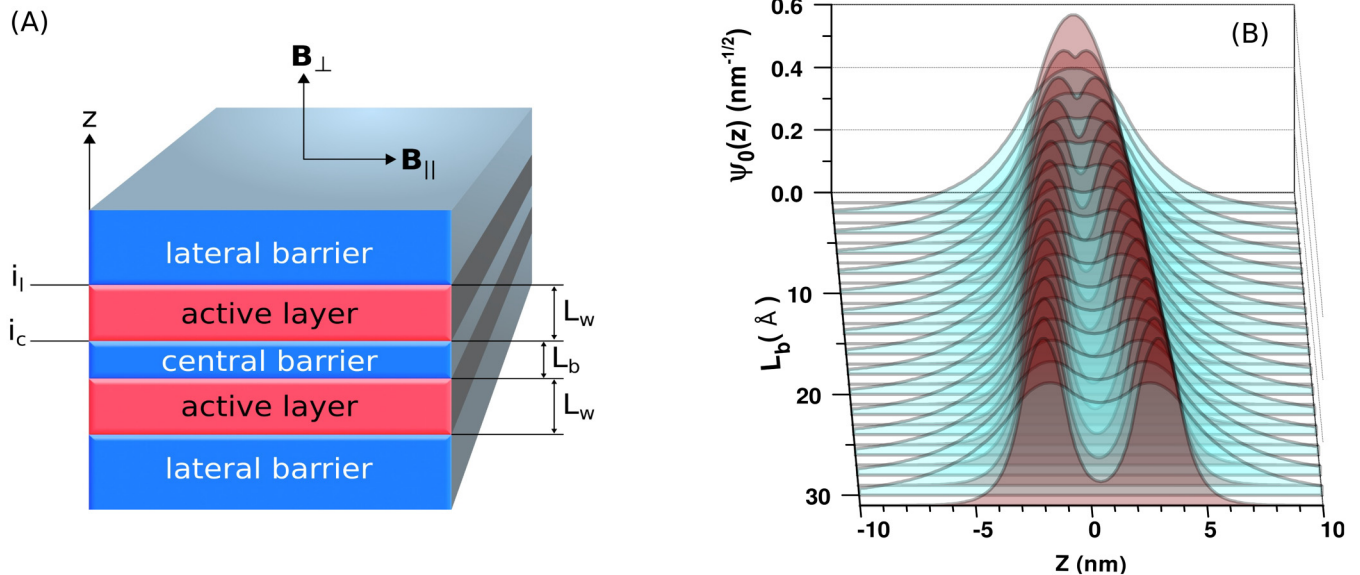


FIG. 2. (a) Symmetric multilayer structure formed by equal active layers with thickness L_w and, between them, a tunnel-coupling (central) barrier formed by the same bulk as the lateral barriers (L_b is the central-barrier width). The z -axis sets the growth direction, i_c indicates interfaces between active layers and the central barrier, i_l is between active layers and lateral barriers; B_{\perp} and B_{\parallel} show magnetic-field configurations. (b) Unperturbed wavefunction varying with L_b , and fixing $L_w = 2$ nm, for the multilayers AlSb|InAs|AlSb|InAs|AlSb and Inp|InGaAs|Inp|InGaAs|Inp represented in wine and cyan, respectively.

18 March 2024 14:57:17

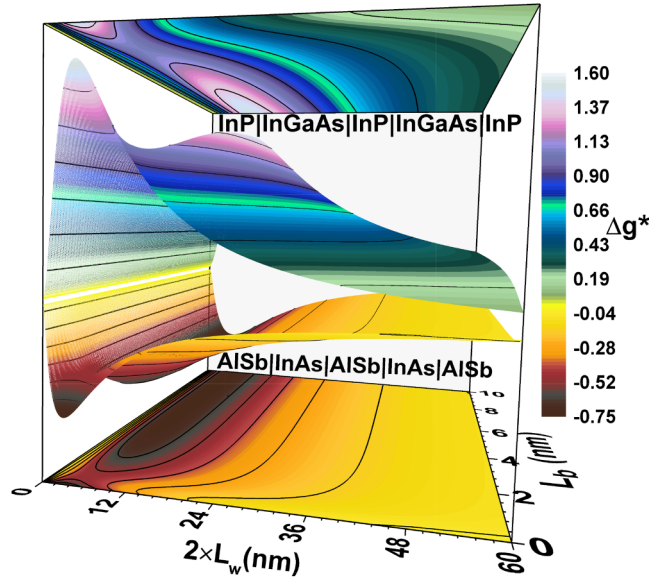


FIG. 3. The contour-plot maps show the electron g -factor anisotropy computed over the whole space spanned (where L_w is the thickness of the active layers and L_b is the central-barrier length), given according to the color legend on the right. The upper surface and its projection (on the top panel) show the results for InP|In_{0.53}Ga_{0.47}As|InP|In_{0.53}Ga_{0.47}As|InP multilayers, for which $\Delta g \geq 0$, and the lower graphics show the results for AISb|InAs|AISb|InAs|AISb, for which $\Delta g \leq 0$.

For completeness and support our results, in Fig. 4, we present parallel and perpendicular components of the electron g -factor tensor obtained from Eqs. (3) and (6), and the corresponding anisotropy as continuous functions of $2L_w$. Varying L_b in units of 0.2 \AA , we create fine grids with individual elements of g_{\parallel}^* , g_{\perp}^* , and Δg^* , starting from $L_b = 0$ to L_b large. For $L_b = 0$, the results reproduce the curves shown in Fig. 1(b) (replacing $L_w \rightarrow 2L_w$ since the multilayer reduces to a single active layer with a thickness of $2L_w$), while L_b increases, the noninteracting limit is reached in AISb|InAs-based structures much faster than the InP|InGaAs-based.

IV. STRUCTURE INVERSION ASYMMETRY

To investigate how the SIA affects the electron g -factor anisotropy in III-V multilayers consistently with our comparative framework, we introduce a single modification of the structure presented in Sec. III, considering one of the lateral barriers as a perfect insulator, while all the other layers are maintained as shown in Fig. 2; this choice preserves the entire parameter set used along this paper, enabling a fair comparison between the results for symmetric and asymmetric structures. Starting from the interface i_0 between the perfect insulator and the active layer, we enumerate the interfaces i_1 , i_2 , and i_3 as shown in Fig. 5. Between i_1 and i_2 , a central barrier separates two interacting active layers: the active layer between i_0 and i_1 is asymmetrically surrounded, while the other active layer, between i_2 and i_3 , is

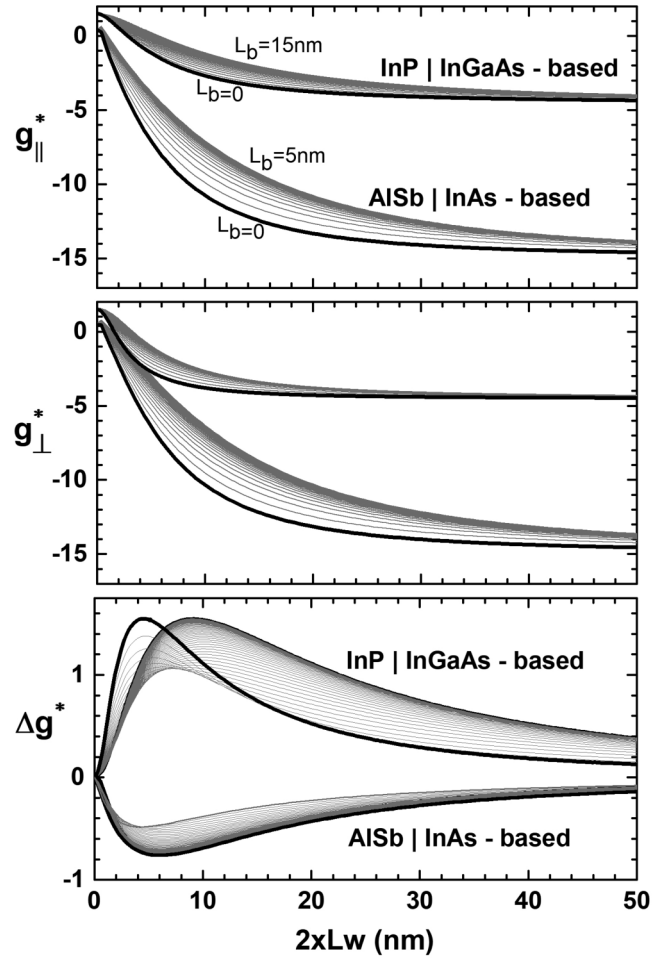


FIG. 4. Parallel and perpendicular components of electron g -factor tensor and the corresponding anisotropy as continuous functions of $2L_w$, considering the structure parameterization shown in Fig. 2. We construct fine grids with individual elements of g_{\parallel}^* , g_{\perp}^* , and Δg^* varying L_b in units of 0.2 \AA , starting from $L_b = 0$ to the noninteracting limit (L_b sufficiently large).

neighbored by barrier layers with the same bulk. With the corresponding boundary conditions, it is easy to find the zero-order solutions ϵ_0 and ψ_0 as shown in Appendix A, particularly noting that $\psi_0(z_{i_0} = 0) = 0$ to calculate the electron g -factor anisotropy as follows:

$$\Delta g^* = (4m_e/\hbar^2) \{ L_b [|\psi_0(z_{i_3})|^2 - |\psi_0(z_{i_2})|^2] + L_w |\psi_0(z_{i_3})|^2 + (L_w - z_0) [|\psi_0(z_{i_3})|^2 - |\psi_0(z_{i_2})|^2 + |\psi_0(z_{i_1})|^2] \} \delta\beta(\epsilon_0). \quad (10)$$

In Fig. 6, we present the results obtained by solving Eq. (10) for Insulator|InGaAs|InP|InGaAs|InP and Insulator|InAs|AISb|InAs|AISb structures, as labeled. The g -factor anisotropy is plotted

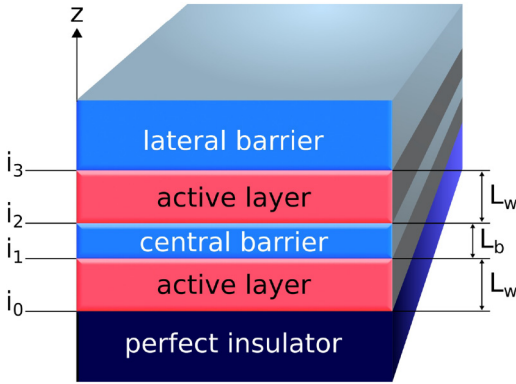


FIG. 5. Scheme of an asymmetric multilayer structure; the z axis sets the growth direction, i_0 , i_1 , i_2 , and i_3 locate the interfaces. Between i_1 and i_2 , a central barrier with thickness L_b separates two equal interacting active layers; however, the active layer between i_0 and i_1 is asymmetrically surrounded, while the other active layer (between i_2 and i_3) is symmetric.

as a continuous function of L_b , varying L_w in units of 0.5 \AA to form a fine grid closed to enlight the sign inversion of Δg^* depending on the active-layer thickness due to the SIA. Such a sign inversion is predicted to happen when the confinement is strong enough to push the average value of the electron position (z_0) out of the confining region ($z_0 > z_i$); since the tunnel coupling competes to reduce the SIA effects, it restricts a possible sign inversion of Δg^* to thin active layers within the strongly interacting regime. Instead, when L_b increases, the electronic ground state will be progressively transferred to the symmetrically neighbored active layer such that the SIA effects must disappear in the noninteracting limit when z_0 will be located at the center of the symmetric active layer at $z = L_b + 1.5 L_w$. Therefore, the difference $\Delta Z_0 = z_0 - L_b - 1.5 L_w$ informs us how fast the system approaches the symmetric ground state (for which $\Delta Z_0 = 0$) when L_b increases, providing a sensor for the SIA effects and a fine-tuning parameter for the electron g -factor anisotropy. It is a realistic (and minimalist) testing platform to tune the g -factor using a spanned parameter space, including bulk, interface, tunnel coupling, and SIA effects, in a unique manner, for each heterostructure.

The upper panel in Fig. 6 shows the specific results for insulator|InGaAs|InP|InGaAs|InP structures, where we explore the main features of the g -factor anisotropy for different confining domains. Starting from the limit for which the system supports bound states,⁴² namely, critical thickness $L_w^{(c)}$, up to $L_w = 1.9 \text{ nm}$, the curves present a sign inversion when L_b varies. Within this range, the SIA becomes prominent and able to invert Δg^* , noting that this effect fades for L_b large enough such that ΔZ_0 vanishes, and the results reproduce the same obtained for a single symmetric active layer. Particularly remarkable, ΔZ_0 radically differs when comparing the specific cases shown in the insets, being drastically suppressed in the structures based on InAs|AlSb due to the large band offset, which turns the SIA effects inaccessible from a practical point of view. This critical difference between the obtained results indicates that the anisotropy can be tuned or controlled by

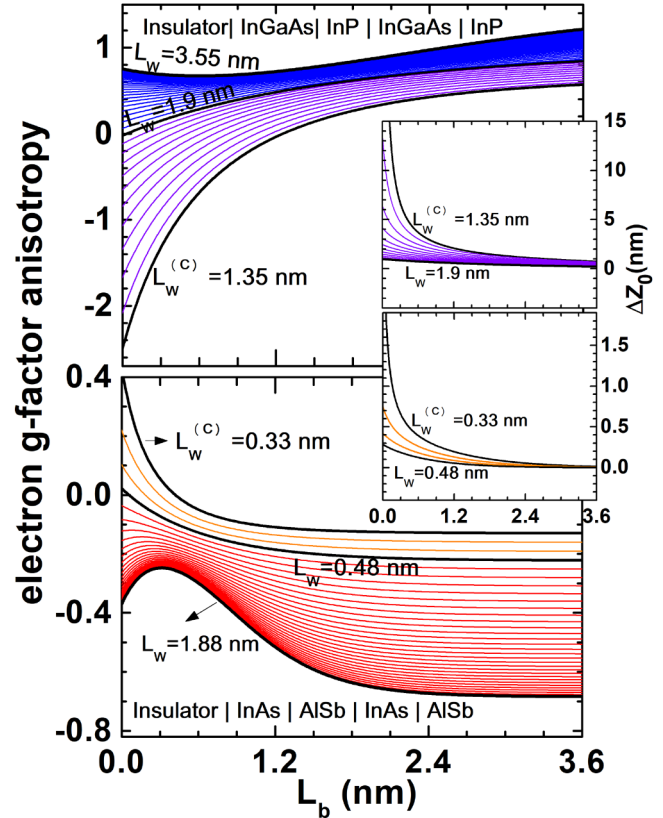


FIG. 6. Electron g -factor anisotropy as a continuous function of L_b , varying L_w in a fine grid with units of 0.5 \AA , starting from the critical thickness $L_w^{(c)}$. The difference $\Delta Z_0 = z_0 - (L_b + 1.5 L_w)$ can be seen as a sensor for the SIA influence on the system. The upper graphics show the results for Insulator|In_{0.53}Ga_{0.47}As|InP|In_{0.53}Ga_{0.47}As|InP structures, and the lower graphics show the results for Insulator|InAs|AlSb|InAs|AlSb.

choosing the structural band offset. Finally, we consider the ranges weakly affected by the SIA effects, between $L_w = 1.9 \text{ nm}$ and $L_w = 3.55 \text{ nm}$ in the upper graphic, and $L_w = 0.48 \text{ nm}$ up to $L_w = 1.88 \text{ nm}$ in the lower panel; in these ranges, the curves reach an interval of leisurely variation with L_w , within a weak confinement regime, until the anisotropy starts to monotonically and slowly decrease (to vanishes in the bulk limit).

To complete our approach, in Fig. 7, we present the g -factor components g_{\parallel}^* , g_{\perp}^* , obtained by solving Eqs. (3) and (6) using the unperturbed analytical solutions found in Appendix A. These results complement those shown in Fig. 6, obtained within the same range and grid parameterization. The noninteracting regime is easily identified for AlSb|InAs-based structures, corresponding to constant g -factor components (when the system reproduces a single symmetric active layer with fixed L_w); contrastingly, the InP|InGaAs-based structures support a broad interacting domain, allowing an additional tunability of the g -factor components.

18 March 2024 14:57:17

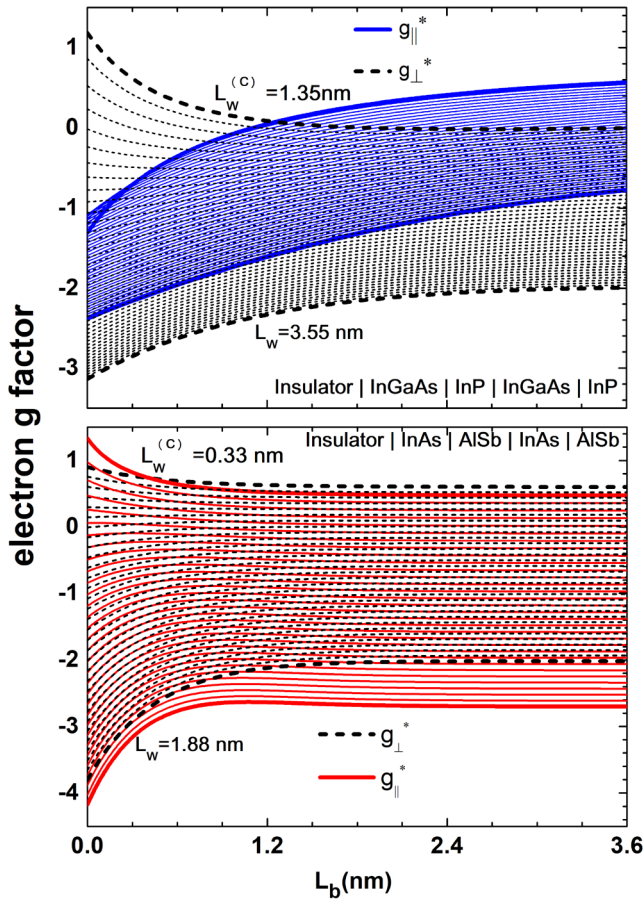


FIG. 7. Components $g_{||}^*$ and g_{\perp}^* of the electron g -factor tensor plotted within the same grid used in Fig. 6, i.e., as continuous functions of L_b , while L_w increases in units of 0.5 \AA , from the critical thickness $L_w^{(c)}$. The graphics are labeled to distinguish results according to the multilayer structure.

V. ADDITIONAL REMARKS

From the theoretical point of view, there are well-established approaches to studying the electron g factor and its anisotropy, including models with 14 bands,¹⁶ elaborated numerical calculations,¹⁴ and tight-binding-based methods.²⁹ In good qualitative agreement with these approaches, the theory explored in this paper represents an alternative analytical framework suitable to include fine structural details as different renormalization mechanisms that affect the g -factor anisotropy, allowing a simple and transparent physical interpretation. With the introduction of the preliminary concepts,¹⁸ such a theoretical view provided elements to later extensions describing the electron g -factor tensor in IV–VI quantum wells,²¹ nitride-based heterostructures,²⁷ and GaAs nanodisks.²⁰ We also recall the good agreement obtained in the previous papers,^{18,30} with independent experimental works involving different techniques, such as time-resolved luminescence spectroscopy,¹³ Larmor beat measurements,¹⁵ and electron spin resonance,¹² taking

into account their respective samples with specific materials and conditions.

Central aspects of the electron g -factor anisotropy are known for some typical III–V heterostructures, remaining incomplete a significant part of the knowledge regarding specific semiconducting matchings, interfacings, and structural details that can drive the electron g -factor anisotropy, to manipulate its sign and eventual sign inversion. It was remarkably studied and well-discussed by Tomimoto *et al.*,¹⁷ who measured a g -factor anisotropy inversion in ultra-thin ZnTe nanolayers using the time-resolved Kerr-rotation technique. Despite the difficulty of applying the present theory for structures with relatively large gaps,⁴⁵ our findings show that, besides the appropriate combination of the well and barrier materials and an ultrathin potential well, as reported in Ref. 17, SIA is a fundamental ingredient to induce the g -factor anisotropy inversion by varying the quantum confinement. Foremost, Δg^* depends, in a nonmonotonic way, on the difference between SO coefficients associated with heterostructure constituents, wave function penetration into the barrier materials, tunnel coupling between active layers, and SIA effects. For this reason, we point out the testing platforms for Majorana devices⁴⁴ as promising to study the electron g -factor anisotropy since the tunnel coupling and SIA effects are boosted due to a tiny band offset ($\approx 86 \text{ meV}$, as reported) together with a narrow-gap active layer.

VI. SUMMARY AND CONCLUSIONS

In summary, we have presented a detailed comparative analysis between the electron g factor anisotropy calculated for realistic heterostructures based on the semiconductor interfaces InGaAs|InP and InAs|AlSb, including the interplay between fine-tuning mechanisms. Effects from interfacial, tunnel coupling, and SIA are progressively introduced and analyzed within a transparent comparative view. Critical differences are identified and explained in terms of the bulk and structural characteristics, as, in particular, (1) the sign of the electron g -factor anisotropy in symmetric structures such that $g_{||} \geq g_{\perp}$ for InGaAs|InP-based structures and $g_{||} \leq g_{\perp}$ for those based on InAs|AlSb, depending on the difference between SO coefficients, as extensively discussed along this paper; (2) breaking the structural inversion symmetry acts to invert the g factor anisotropy in the strong confinement limit (or sufficiently thin layers); however, in InAs|AlSb-heterostructures, the penetration of the electronic wavefunction into the AlSb barriers is suppressed such that the SIA effects become inaccessible from a practical perspective. Our findings show that SIA effects are expected to be prominent in structures with small conduction-band offsets, enabling new possibilities to tune the electron g -factor anisotropy. The results are consistent over the whole parameter space, based on an analytically transparent and yet accurate theoretical approach, easily suitable to a wide range of heterostructures and free for expensive nor advanced computational resources and aims to integrate structural design into g -factor engineering and guide experimental efforts.

ACKNOWLEDGMENTS

The authors acknowledge financial support from the funding agencies: CNPq [Project Nos. 306145/2018-9, and

18 March 2024, 14:57:17

No. 442493/2019-3 (Process No. 383389/2022-4)], CAPES (No. PNPB 88882.306206/2018-01), and Office of Naval Research (Global office in South America, NICOP) Grant No. N62909-18-1-2121. M.A.T. Sandoval acknowledges Dr. E. A. de Andrada e Silva for appraising discussions.

AUTHOR DECLARATIONS

Conflict of Interest

The authors have no conflicts to disclose.

Author Contributions

M. A. Toloza Sandoval: Conceptualization (lead); Formal analysis (equal); Writing – original draft (lead). **J. E. Leon Padilla:** Formal analysis (equal); Investigation (equal); Methodology (equal). **A. B. Wanderley:** Data curation (equal); Software (equal); Visualization (equal). **G. M. Sipahi:** Formal analysis (supporting); Methodology (supporting); Writing – review & editing (equal). **J. F. Diniz Chubaci:** Formal analysis (equal); Resources (equal). **A. Ferreira da Silva:** Project administration (lead); Supervision (lead); Writing – review & editing (equal).

DATA AVAILABILITY

The data that support the findings of this study are available within the article.

APPENDIX A: UNPERTURBED SOLUTION INCLUDING SIA

In this appendix, we provide the analytical expressions for the zero-order (unperturbed) solutions used in Sec. IV; this information complements the Hamiltonian formulation and the perturbation theory extensively discussed in Refs. 26 and 30. Considering the structure described in Fig. 5, the choice of the interface i_0 between the perfect insulator and the active layer as the origin of the coordinate system, i.e., $z_{i_0} = 0$, is adequate to apply the boundary conditions [in particular, $\psi_0(z) = 0$ if $z \leq 0$], leading to the solutions,

$$\psi_0(z) = \left\{ \begin{array}{ll} \mathcal{A} \sin(k_w z), & 0 \leq z \leq L_w \\ \mathcal{B} e^{k_b z} + \mathcal{C} e^{-k_b z}, & L_w \leq z \leq L_w + L_b \\ \mathcal{D} \cos(k_w z) + \mathcal{E} \sin(k_w z), & L_w + L_b \leq z \leq 2L_w + L_b \\ \mathcal{F} e^{-k_b z}, & z \geq 2L_w + L_b \end{array} \right\}, \quad (\text{A1})$$

and the unperturbed energy ϵ_0 is obtained by solving the following transcendental equation:

$$\tanh \Theta_b = \frac{\xi \sin 2\Theta_w + \cos 2\Theta_w}{\left(\frac{1}{\xi} - \xi\right) \sin \Theta_w \cos \Theta_w - \cos^2 \Theta_w - \xi^2 \sin^2 \Theta_w}, \quad (\text{A2})$$

where $\Theta_b = k_b L_b$, $\Theta_w = k_w L_w$, and $\xi = k_b m_w / (k_w m_b)$, and the coefficients \mathcal{A} , \mathcal{B} , \mathcal{C} , \mathcal{D} , \mathcal{E} , and \mathcal{F} are obtained from the normalization condition, completing the theoretical framework employed in this paper.

REFERENCES

- 1 S. Tomonaga, *The Story of Spin* (University of Chicago Press, 1997).
- 2 See, for instance, M. Maggiore, *A Modern Introduction to Quantum Field Theory* (Oxford University Press, 2005).
- 3 A. Fert and F. N. Van Dau, "Spintronics, from giant magnetoresistance to magnetic skyrmions and topological insulators," *C. R. Phys.* **20**, 817–831 (2019).
- 4 L. M. Roth, B. Lax, and S. Zwerdling, "Theory of optical magneto-absorption effects in semiconductors," *Phys. Rev.* **114**, 90 (1959).
- 5 H. Kosaka, A. Kiselev, F. Baron, K. Wook Kim, and E. Yablonovitch, "Electron g factor engineering in III-V semiconductors for quantum communications," *Electron. Lett.* **37**, 464–465 (2001).
- 6 H. C. Koo, J. H. Kwon, J. Eom, J. Chang, S. H. Han, and M. Johnson, "Control of spin precession in a spin-injected field effect transistor," *Science* **325**, 1515–1518 (2009).
- 7 R. M. Lutchyn, E. P. A. M. Bakkers, L. P. Kouwenhoven, P. Krogstrup, C. M. Marcus, and Y. Oreg, "Majorana zero modes in superconductor/semiconductor heterostructures," *Nat. Rev. Mater.* **3**, 52–68 (2018).
- 8 Y. Jiang, E. Maksim, G. Kipshidze, S. Moon, M. Ozerov, D. Smirnov, Z. Jiang, and S. Suchalkin, "Giant g -factors and fully spin-polarized states in metamorphic short-period InAsSb/InSb superlattices," *Nat. Commun.* **13**, 5960 (2022).
- 9 J.-M. Jancu, R. Scholz, E. A. de Andrada e Silva, and G. C. La Rocca, "Atomistic spin-orbit coupling and $\mathbf{k} \cdot \mathbf{p}$ parameters in III-V semiconductors," *Phys. Rev. B* **72**, 193201 (2005).
- 10 C. M. O. Bastos, F. P. Sabino, G. M. Sipahi, and J. L. F. Da Silva, "A comprehensive study of g -factors, elastic, structural and electronic properties of III-V semiconductors using hybrid-density functional theory," *J. Appl. Phys.* **123**, 065702 (2018).
- 11 "Semiconductors: Intrinsic properties of group IV elements and III-V, II-VI and I-VII compounds," in *Landolt-Bornstein New Series*, edited by O. Madelung (Springer, Berlin, 1987), Vol. III/22a.
- 12 B. Kowalski, P. Omling, B. K. Meyer, D. M. Hofmann, C. Wetzel, V. Härle, F. Scholz, and P. Sobkowicz, "Conduction-band spin splitting of type-I $\text{Ga}_x\text{In}_{1-x}\text{As}/\text{InP}$ quantum wells," *Phys. Rev. B* **49**, 14786–14789 (1994).
- 13 P. Le Jeune, D. Robart, X. Marie, T. Amand, M. Brosseau, J. Barrau, and V. Kalevich, "Anisotropy of the electron Landé g factor in quantum wells," *Semicond. Sci. Technol.* **12**, 380 (1997).
- 14 A. A. Kiselev, E. L. Ivchenko, and U. Rössler, "Electron g factor in one- and zero-dimensional semiconductor nanostructures," *Phys. Rev. B* **58**, 16353–16359 (1998).
- 15 A. Malinowski and R. T. Harley, "Anisotropy of the electron g factor in lattice-matched and strained-layer III-V quantum wells," *Phys. Rev. B* **62**, 2051–2056 (2000).
- 16 P. Pfeffer and W. Zawadzki, "Anisotropy of spin g factor in $\text{GaAs}/\text{Ga}_{1-x}\text{Al}_x\text{As}$ symmetric quantum wells," *Phys. Rev. B* **74**, 233303 (2006).
- 17 S. Tomimoto, S. Nozawa, Y. Terai, S. Kuroda, K. Takita, and Y. Masumoto, "Anisotropic spin dynamics of confined electrons in CdTe/ZnTe quantum structures," *Phys. Rev. B* **81**, 125313 (2010).
- 18 M. A. Toloza Sandoval, A. Ferreira da Silva, E. A. de Andrada e Silva, and G. C. La Rocca, "Mesoscopic spin-orbit effect in the semiconductor nanostructure electron g factor," *Phys. Rev. B* **86**, 195302 (2012).
- 19 S. Takahashi, R. S. Deacon, A. Oiwa, K. Shibata, K. Hirakawa, and S. Tarucha, "Electrically tunable three-dimensional g -factor anisotropy in single InAs self-assembled quantum dots," *Phys. Rev. B* **87**, 161302 (2013).
- 20 L.-W. Yang, Y.-C. Tsai, Y. Li, A. Higo, A. Murayama, S. Samukawa, and O. Voskoboinikov, "Tuning of the electron g factor in defect-free GaAs nanodisks," *Phys. Rev. B* **92**, 245423 (2015).
- 21 E. Ridolfi, E. A. de Andrada e Silva, and G. C. La Rocca, "Effective g -factor tensor for carriers in IV-VI semiconductor quantum wells," *Phys. Rev. B* **91**, 085313 (2015).
- 22 A. V. Shchepetilnikov, Y. A. Nefyodov, I. V. Kukushkin, L. Tiemann, C. Reichl, W. Dietsche, and W. Wegscheider, "Electron g -factor anisotropy in an AlAs quantum well probed by ESR," *Phys. Rev. B* **92**, 161301 (2015).

18 March 2024, 14:57:17

- ²³M. Pakmehr, A. Khaetskii, B. D. McCombe, N. Bhandari, M. Cahay, O. Chiatti, S. F. Fischer, C. Heyn, and W. Hansen, "The g -factor of quasi-two-dimensional electrons in InAs/InGaAs/InAlAs inserted-channels," *Appl. Phys. Lett.* **107**, 082107 (2015).
- ²⁴V. V. Belykh, D. R. Yakovlev, J. J. Schindler, E. A. Zhukov, M. A. Semina, M. Yacob, J. P. Reithmaier, M. Benyoucef, and M. Bayer, "Large anisotropy of electron and hole g factors in infrared-emitting InAs/InGaAs self-assembled quantum dots," *Phys. Rev. B* **93**, 125302 (2016).
- ²⁵F. Qu, J. van Veen, F. K. de Vries, A. J. A. Beukman, M. Wimmer, W. Yi, A. A. Kiselev, B.-M. Nguyen, M. Sokolich, M. J. Manfra, F. Nichele, C. M. Marcus, and L. P. Kouwenhoven, "Quantized conductance and large g -factor anisotropy in InSb quantum point contacts," *Nano Lett.* **16**, 7509–7513 (2016).
- ²⁶M. A. T. Sandoval, E. A. de Andrada e Silva, A. F. da Silva, and G. C. L. Rocca, "Electron g factor anisotropy in asymmetric III-V semiconductor quantum wells," *Semicond. Sci. Technol.* **31**, 115008 (2016).
- ²⁷M. Li, Z.-B. Feng, L. Fan, Y. Zhao, H. Han, and T. Feng, "The electron g factor in AlGaIn/GaN quantum wells," *J. Magn. Magn. Mater.* **403**, 81–85 (2016).
- ²⁸F. Herzog, H. Hardtdegen, T. Schäpers, D. Grundler, and M. A. Wilde, "Experimental determination of Rashba and Dresselhaus parameters and g^* -factor anisotropy via Shubnikov-de Haas oscillations," *New J. Phys.* **19**, 103012 (2017).
- ²⁹A. Tadjine, Y.-M. Niquet, and C. Delerue, "Universal behavior of electron g -factors in semiconductor nanostructures," *Phys. Rev. B* **95**, 235437 (2017).
- ³⁰M. A. T. Sandoval, J. E. Leon Padilla, A. Ferreira da Silva, E. A. de Andrada e Silva, and G. C. La Rocca, "Mesoscopic g -factor renormalization for electrons in III-V interacting nanolayers," *Phys. Rev. B* **98**, 075312 (2018).
- ³¹In the weak magnetic-field limit, the parabolic potential becomes negligible compared with the electronic confinement due to the conduction band offsets; nevertheless, the electronic ground state presents a significant (effective Zeeman) spin-splitting obtained using first-order perturbation theory.
- ³²L. Gerchikov and A. Subashiev, "Spin splitting of size-quantization subbands in asymmetric heterostructures," *Sov. Phys. Semicond.* **26**, 73 (1992).
- ³³E. A. de Andrada e Silva, G. L. Rocca, and F. Bassani, "Spin-orbit splitting of electronic states in semiconductor asymmetric quantum wells," *Phys. Rev. B* **55**, 16293–16299 (1997).
- ³⁴F. Vasko and A. Kuznetsov, *Electronic States and Optical Transitions in Semiconductor Heterostructures*, Graduate Texts in Contemporary Physics (Springer, New York, 1998).
- ³⁵Within the perturbative approach, i.e., weak magnetic-field limit, the electronic effective mass varies with the confining energy (ϵ) and the position (z) along the growth direction, and its dependence on the magnetic field is neglected.
- ³⁶G. Bastard, *Wave Mechanics Applied to Semiconductor Heterostructures*, Monographies de physique (Les Éditions de Physique, Les Ulis, 1990).
- ³⁷L. Voon and M. Willatzen, *The $k \cdot p$ Method: Electronic Properties of Semiconductors* (Springer, Berlin, 2009).
- ³⁸This contribution includes all the (remote) bands not included in the eight-band Kane model; it is given by the difference between experimental g factors and the values obtained from Roth's formula, and the dependence on z does indicate the layer (material) along the structure.
- ³⁹E. A. de Andrada e Silva, G. C. La Rocca, and F. Bassani, "Spin-split subbands and magneto-oscillations in III-V asymmetric heterostructures," *Phys. Rev. B* **50**, 8523–8533 (1994).
- ⁴⁰I. A. Yugova, A. Greulich, D. R. Yakovlev, A. A. Kiselev, M. Bayer, V. V. Petrov, Y. K. Dolgikh, D. Reuter, and A. D. Wieck, "Universal behavior of the electron g factor in GaAs/Al_xGa_{1-x}As," *Phys. Rev. B* **75**, 245302 (2007).
- ⁴¹In the zero magnetic field limit $B \rightarrow 0$, z_0 gives the center of the cyclotron orbit, i.e., $z_0 \rightarrow -\hbar k_x / eB$.
- ⁴²In contrast to symmetric structures, which support bound states when L_w approaches zero, the asymmetric structures present a confinement limit for bound states (the critical thickness $L_w^{(c)}$).
- ⁴³For these structures, the k -cubic corrections cannot be neglected.
- ⁴⁴D. Car, S. Conesa-Boj, H. Zhang, R. L. M. Op Het Veld, M. W. A. de Moor, E. M. T. Fadaly, Ö. Gül, S. Kölling, S. R. Plissard, V. Toresen, M. T. Wimmer, K. Watanabe, T. Taniguchi, L. P. Kouwenhoven, and E. P. A. M. Bakkers, "InSb nanowires with built-in Ga_xIn_{1-x}Sb tunnel barriers for majorana devices," *Nano Lett.* **17**, 721–727 (2017).